

## Amorphization of Ta<sub>2</sub>O<sub>5</sub> under swift heavy ion irradiation

Alex B. Cusick<sup>a</sup>, Maik Lang<sup>b</sup>, Fuxiang Zhang<sup>c</sup>, Kai Sun<sup>a</sup>, Weixing Li<sup>d</sup>, Patrick Kluth<sup>e</sup>, Christina Trautmann<sup>f,g</sup>, Rodney C. Ewing<sup>a,c,d,\*</sup>

<sup>a</sup> Materials Science & Engineering, University of Michigan, Ann Arbor, MI 48109, USA

<sup>b</sup> Nuclear Engineering, University of Tennessee, Knoxville, TN 37996, USA

<sup>c</sup> Earth & Environmental Sciences, University of Michigan, Ann Arbor, MI 48109, USA

<sup>d</sup> Geological Sciences, Stanford University, Stanford, CA 94305, USA

<sup>e</sup> Research School of Physics and Engineering, Australian National University, Canberra ACT 2601, Australia

<sup>f</sup> GSI Helmholtz Centre for Heavy Ion Research, D-64291 Darmstadt, Germany

<sup>g</sup> Technische Universität Darmstadt, 64287 Darmstadt, Germany

### ARTICLE INFO

#### Article history:

Received 20 April 2017

Accepted 18 May 2017

#### Keywords:

Swift heavy ions

Irradiation

Phase transformation

Tantalum oxide

Amorphization

### ABSTRACT

Crystalline Ta<sub>2</sub>O<sub>5</sub> powder is shown to amorphize under 2.2 GeV <sup>197</sup>Au ion irradiation. Synchrotron X-ray diffraction (XRD), Raman spectroscopy, small-angle X-ray scattering (SAXS), and transmission electron microscopy (TEM) were used to characterize the structural transition from crystalline to fully-amorphous. Based on Rietveld refinement of XRD data, the initial structure is orthorhombic (*P2mm*) with a very large unit cell ( $a = 6.20$ ,  $b = 40.29$ ,  $c = 3.89$  Å;  $V = 971.7$  Å<sup>3</sup>), ideally containing 22 Ta and 55 O atoms. At a fluence of approximately  $3 \times 10^{11}$  ions/cm<sup>2</sup>, a diffuse amorphous background becomes evident, increasing in intensity relative to diffraction maxima until full amorphization is achieved at approximately  $3 \times 10^{12}$  ions/cm<sup>2</sup>. An anisotropic distortion of the orthorhombic structure occurred during the amorphization process, with an approximately constant unit cell volume. The amorphous phase fraction as a function of fluence was determined, yielding a trend that is consistent with a direct-impact model for amorphization. SAXS and TEM data indicate that ion tracks exhibit a core-shell morphology. Raman data show that the amorphous phase is comprised of TaO<sub>6</sub> and TaO<sub>5</sub> coordination-polyhedra in contrast to the TaO<sub>6</sub> and TaO<sub>7</sub> units that exist in crystalline Ta<sub>2</sub>O<sub>5</sub>. Analysis of Raman data shows that oxygen-deficiency increases with fluence, indicating a loss of oxygen that leads to an estimated final stoichiometry of Ta<sub>2</sub>O<sub>4.2</sub> at a fluence of  $1 \times 10^{13}$  ions/cm<sup>2</sup>.

© 2017 Elsevier B.V. All rights reserved.

### 1. Introduction

Ta<sub>2</sub>O<sub>5</sub> is a complex and versatile material that has many applications in materials engineering. One of the most notable characteristics of Ta<sub>2</sub>O<sub>5</sub> is its high dielectric constant (relative permittivity) [1–11], which has an unusually high value in the range of 25–100 depending on processing factors such as synthesis methodology and annealing temperature [1]. Although the crystalline state has a higher absolute dielectric constant than the amorphous phase (ranging from 56 to 59) [12], it is highly anisotropic. Therefore, the amorphous form is often used in microelectronics in order to avoid this effect [7]. The amorphous form also

exhibits improved leakage current properties due to the decreased loss at grain boundaries [13]. The high dielectric constant, high dielectric breakdown strength [2], and good leakage current properties [2,14] make Ta<sub>2</sub>O<sub>5</sub> a useful material for gate dielectrics in transistors [1,6], dielectric resonators in microwave communication devices [1], and charge capacitors in dynamic RAM devices [5]. Due to these properties, Ta<sub>2</sub>O<sub>5</sub> is also regarded as one of the best candidate materials to replace conventional SiO<sub>2</sub> and Si<sub>3</sub>N<sub>4</sub> thin-film circuit devices [12]. This is because Si containing materials have reached their physical limit for size reduction [12] and use of Ta<sub>2</sub>O<sub>5</sub> will allow the down-scaling that future microelectronic devices will rely on [4].

Tantalum pentoxide is also widely used due to its optical properties, typically in the amorphous state, in order to avoid scattering loss at grain boundaries [7]. Ta<sub>2</sub>O<sub>5</sub> is commonly used as a coating on solar cells due to its high refractive index, forming a low loss, anti-reflective layer that increases cell efficiency [1,5,7,8,15]. This material is used in optical waveguides [6], electroluminescent dis-

\* Corresponding author at: Geological Sciences, Stanford University, Stanford, CA 94305-2115, USA.

E-mail addresses: [acusick@umich.edu](mailto:acusick@umich.edu) (A.B. Cusick), [mlang2@utk.edu](mailto:mlang2@utk.edu) (M. Lang), [zhangfx@umich.edu](mailto:zhangfx@umich.edu) (F. Zhang), [kaisun@umich.edu](mailto:kaisun@umich.edu) (K. Sun), [wqli@stanford.edu](mailto:wqli@stanford.edu) (W. Li), [Patrick.kluth@anu.edu.au](mailto:Patrick.kluth@anu.edu.au) (P. Kluth), [c.trautmann@gsi.de](mailto:c.trautmann@gsi.de) (C. Trautmann), [rewing1@stanford.edu](mailto:rewing1@stanford.edu) (R.C. Ewing).

plays [6], and also as a photocatalyst [8,15,16]. In addition, it is utilized as a chemical catalyst [7], gas sensor [5,15], proton conductor [7], and in surface acoustic wave devices [6]. As the structure highly affects its usefulness, the crystalline-to-amorphous transition is of great interest.

The structures of various polymorphs are not well defined for  $\text{Ta}_2\text{O}_5$ , largely due to the complexity of their crystallization behavior. There are two common ambient pressure structures, the low temperature L- $\text{Ta}_2\text{O}_5$  (or  $\beta\text{-Ta}_2\text{O}_5$ ) phase and high temperature H- $\text{Ta}_2\text{O}_5$  (or  $\alpha\text{-Ta}_2\text{O}_5$ ) phase. L- $\text{Ta}_2\text{O}_5$  is generally considered to be orthorhombic [17–20], comprised of corner- and edge-sharing  $\text{TaO}_6$  octahedra and  $\text{TaO}_7$  pentagonal bipyramids [21]. A monoclinic model has also been proposed [17]. Although many unit cell parameters have been reported, the value of the longest parameter varies greatly, ranging from approximately 3.66 Å [22] to over 69.55 Å [17] in order to obtain cell symmetry. One of the most widely accepted models, given by Stephenson & Roth [20], is orthorhombic ( $P2mm$ ) with dimensions:  $a = 6.20$ ,  $b = 40.29$ ,  $c = 3.89$  Å. This model contains 11 formula units and relies on several O-vacancies and/or Ta-interstitials for charge neutrality; a representation of this structure is shown in Fig. 1.

A hexagonal structure,  $\delta\text{-Ta}_2\text{O}_5$  [23,24], has also been reported and is thought to be stable at ambient conditions along with L- $\text{Ta}_2\text{O}_5$ . This phase has been shown to have tantalum coordination numbers of both 6 and 8 [25], which has been confirmed by computational simulations of the structure [26]. Transformation of  $\delta\text{-Ta}_2\text{O}_5$  into an orthorhombic structure occurs upon heating to 900 °C [23]. At temperatures above  $\sim 1340$  °C, L- $\text{Ta}_2\text{O}_5$  transforms to H- $\text{Ta}_2\text{O}_5$  [5,19]. This structure is often considered to be orthorhombic [27,28], though it apparently has several variants including tetragonal [22,28,29], monoclinic [1,21,22,30], and triclinic [22]. Because the transformation from H- $\text{Ta}_2\text{O}_5$  is slow, and cooling of H- $\text{Ta}_2\text{O}_5$  has been shown to form several intermediate phases [19], it is difficult to prepare high quality L- $\text{Ta}_2\text{O}_5$  crystals by conventional high-temperature methods.

Two main high-pressure phases have been reported, both with monoclinic structures. B- $\text{Ta}_2\text{O}_5$  is comprised of  $\text{TaO}_6$  polyhedra only [31]; whereas, Z- $\text{Ta}_2\text{O}_5$  consists of  $\text{TaO}_7$  polyhedra only [24,31]. These two structures are closely related, easily transforming from one to the other, and a mixture of the two structures has been shown to form at 8 GPa and 1197 °C [31]. Another monoclinic phase has been shown to form at 297–347 °C and 20 MPa, denoted  $\epsilon\text{-Ta}_2\text{O}_5$  [24], which is 6-coordinated and is likely equivalent to B- $\text{Ta}_2\text{O}_5$ . This  $\epsilon\text{-Ta}_2\text{O}_5$  phase has been shown to irreversibly transform into L- $\text{Ta}_2\text{O}_5$  at 887 °C [24]. Transformation from a monoclinic to trigonal structure has also been observed by very slow cooling from 1000 °C [32].

Materials subjected to swift heavy ion irradiation undergo complex structural modifications at the nano-scale; the extent of modification is dependent on the material as well as the ion species and energy. The effects on relatively radiation-resistant materials consist of defect production and clustering, grain growth, fragmenta-

tion, swelling, and polygonization [33,34]. In materials with a higher susceptibility to damage accumulation, the effects include crystalline-to-crystalline phase transformations (often into high temperature or high pressure phases) [35–38], amorphization [2,36,39–43], and cation reduction with associated anion loss [44–48]. Because the properties of a material are so highly dependent on structure, nano-scale structure modifications using ion beams are of great interest.

Swift heavy ions are highly charged heavy atoms accelerated to energies of over 1 MeV/nucleon (often in the GeV range). As the ions bombard a target material, their energy is deposited into the material's electronic subsystem, causing intense electronic excitation and ionization as the ions slow. This energy deposition (ion energy loss, represented by  $dE/dx$ ) is concentrated in a very small cylindrical volume, with radii of a few nanometers around the ion's trajectory, resulting in extremely high energy densities. The subsequent transfer of energy to the atomic lattice induces a cylindrical damage zone, termed an "ion track". Although there have been many models proposed, there exists no single theory that describes all aspects of ion track formation. According to the thermal-spike model, energy from the electronic subsystem is transferred to atoms within the lattice through electron-phonon coupling, causing a sharp increase in temperature throughout the ion track [49–52]. This high-temperature transient results in the melting or vaporization of material within this region, leaving behind a highly modified and defective structure (often amorphous) after rapid quenching to the bulk. This model also provides a framework for understanding the high-temperature and high-pressure phase formation during irradiation, as rapid kinetics may lead to crystallization of these structures during the transient. The Coulomb-explosion model provides an alternative model for track formation, and focuses on the massive charge separation caused by dense ionization, inducing strong electro-static forces that displace atoms from their sites [53–55]. Alternative models have also been proposed, that describe damage formation based on the decay of self-trapped excitons [56,57] and bond-weakening [58,59].

Ion tracks are typically on the order of several nanometers in diameter and many microns in length. This geometry is unique to swift heavy ion effects. Due to the significance of  $\text{Ta}_2\text{O}_5$  in engineering applications, nanoscale modifications to its structure may have significant technological implications. This paper describes the first swift heavy ion irradiation study of crystalline  $\text{Ta}_2\text{O}_5$ , which leads to amorphization along the ion tracks. Synchrotron-XRD data were obtained for detailed structural characterization over a wide fluence regime, Raman spectroscopy for details on short-range order modifications, along with SAXS and TEM analyses for ion track and grain morphology characterization.

## 2. Experimental methods

Tantalum(V) oxide powder was obtained from MTI Corporation with a theoretical density of 8.2 g/cm<sup>3</sup> and particle sizes on

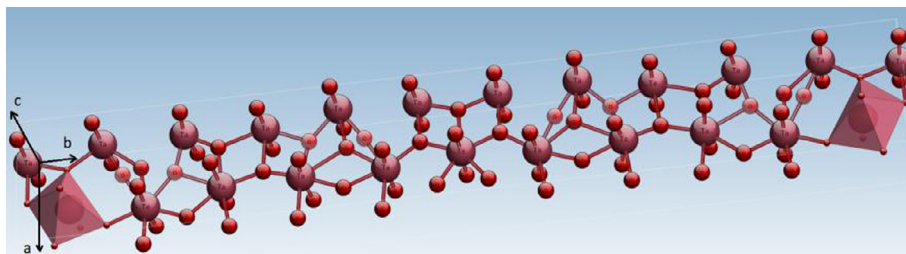


Fig. 1. Orthorhombic structure model proposed by Stephenson & Roth [20], comprised of  $\text{TaO}_6$  and  $\text{TaO}_7$  polyhedra.

the order of 5–10  $\mu\text{m}$ . Sample holders were fabricated by drilling sets of 130  $\mu\text{m}$  diameter holes, using electron discharge machining, into 12.5  $\mu\text{m}$  thick molybdenum foils. The powder was then pressed into these holes using a hydraulic press with a pressure of 20 MPa. This formed sets of cylindrical sample pellets held within the foils, each approximately 130  $\mu\text{m}$  in diameter and 12.5  $\mu\text{m}$  thick. Each set contained seven samples for redundancy, in the event that pellets were lost from the foils during transportation, irradiation, or characterization. Further detail of the sample preparation method can be found in Ref. [60]. Ten sets of samples were prepared and irradiated with 2.2 GeV  $^{197}\text{Au}$  ions (11.1 MeV/u) at room temperature, using the UNILAC linear accelerator at the GSI Helmholtz Centre for Heavy Ion Research in Darmstadt, Germany. Each set was irradiated to a different fluence, increasing from  $5 \times 10^{10}$  to  $1 \times 10^{13}$  ions/cm<sup>2</sup>. The flux was kept sufficiently low to avoid sample heating during irradiation, which was on average  $4 \times 10^9$  ions/cm<sup>2</sup>·s. SRIM code [61] simulations indicated a projected ion range of approximately 58  $\mu\text{m}$  (with a straggle of 1.13  $\mu\text{m}$ ) based on the material's theoretical density. Therefore, all incident ions passed completely through the sample thickness and are not implanted into the sample. The electronic stopping power, dE/dx, was determined to have an approximately constant profile through the sample thickness, with an average value of  $43.5 \pm 1.0$  keV/nm.

Post-irradiation analysis included synchrotron XRD with high energy X-rays ( $\lambda = 0.496$  Å) at the Advanced Photon Source (APS), Argonne National Laboratory. Data were collected from several sample pellets irradiated to each fluence level, including unirradiated samples. Measurements were performed in transmission mode using a MAR345 image plate, with an X-ray spot size of  $4.5 \times 12$   $\mu\text{m}$  (at FWHM) and an exposure time of 120 s [60]. The diffraction images were integrated with Fit2D software [62]. The unirradiated sample diffraction patterns were then quantitatively analyzed using Rietveld refinement conducted with FullProf software [63], in order to characterize the initial structure. Deconvolution of each XRD profile, by manually fitting peaks with Pseudo-Voigt functions, allowed the quantitative separation of intensity contributions from diffraction maxima and amorphous backgrounds (see [64]). Because the relative quantities of the crystalline and amorphous phases are proportional to the relative diffraction pattern area contribution, an “amorphous fraction” was determined for each fluence by calculating the area ratio of amorphous peaks vs. the total pattern area (the sum of amorphous and crystalline peak areas). Peak positions were used to calculate the orthorhombic unit cell parameters as a function of fluence, using the UnitCell code [65].

Raman measurements were performed in backscattering geometry with a red-orange solid state laser ( $\lambda = 633$  nm) and 20 $\times$  microscope objective. The laser power was limited to 0.64 mW to avoid thermal effects during the 40 s exposure times. Several measurements were performed on samples irradiated to all fluences, and analysis of this data was conducted using a deconvolution and peak-fitting procedure. Samples at various fluences were then dispersed onto holey carbon films supported by Cu grids for TEM characterization. Imaging and selected area diffraction was completed using an FEI Tecnai G2 F20 X-TWIN TEM with the field emission gun operated at 200 keV. SAXS data were collected in transmission mode from samples irradiated to  $5 \times 10^{10}$  ion/cm<sup>2</sup> at the SAXS/WAXS beamline at the Australian Synchrotron, using 11 keV X-rays and a camera length of approximately 1600 mm. Spectra were collected using a Pilatus 1 M detector and exposure times of 5 and 10 s. More details on SAXS measurements of ion tracks using this beamline can be found in Ref. [66,67].

### 3. Results

#### 3.1. XRD analysis

The evolution of the diffraction patterns as a function of fluence is shown in Fig. 2. The unirradiated sample profile was best fit with an orthorhombic structure model ( $P2mm$ ), PDF#: 04-007-0695, published by Stephenson & Roth in 1971 [20]. Thus, the initial phase is considered to be pure with no contamination or other phases observed. Manual peak fitting was used to track the positions and widths of the crystalline phase diffraction maxima as the fluence increased, as well as the amorphous background as it increased in intensity. The diffraction maxima broaden with increasing fluence due to the accumulation of defects and microstrain during irradiation. The maxima corresponding to (001), (1, 11, 0), and (1, 11, 1) shift to higher  $2\theta$  values with increasing fluence, whereas those corresponding to (0, 13, 0) and (211) shift to lower values. Therefore, the two double-peaks (centered around approximately  $9.1^\circ$  and  $11.8^\circ$ ) appear to merge with increasing fluence. These peak shifts were used to determine the change in unit cell parameters using the UnitCell code; the results of which are shown in Fig. 3. The unit cell undergoes an anisotropic distortion during irradiation, where the  $a$  parameter expands while  $b$  and  $c$  parameters contract. The  $a$  parameter changes by approximately 0.40%, the  $b$  parameter by 0.08%, and the  $c$  parameter by 0.29%. The unit cell volume remains approximately constant over the entire fluence range.

At a fluence of  $3 \times 10^{11}$  ions/cm<sup>2</sup>, a diffuse amorphous background becomes evident in the XRD profile. As fluence increases, the intensity of this background increases with respect to the crystalline diffraction maxima. At  $3 \times 10^{12}$  ions/cm<sup>2</sup>, crystalline peaks are no longer evident, indicating that the material has become fully amorphous. The amorphous fraction represents the proportion of amorphous material within the sample as a function of fluence, and is shown in Fig. 4. Errors were determined using the standard deviation of five separate Pseudo-Voigt function fits used to calculate the average amorphous fractions. Three mathematical models were used to determine a best-fit to this data: direct-impact, double-overlap, and direct-impact/defect-stimulated models. These models and corresponding mechanisms are discussed in detail by Weber et al. [39].

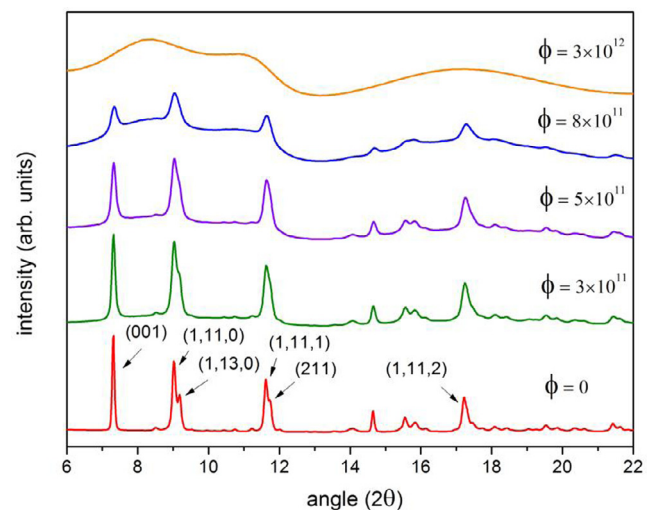
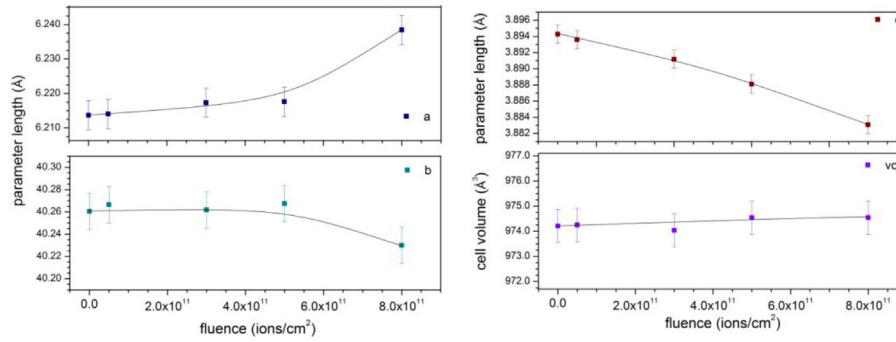
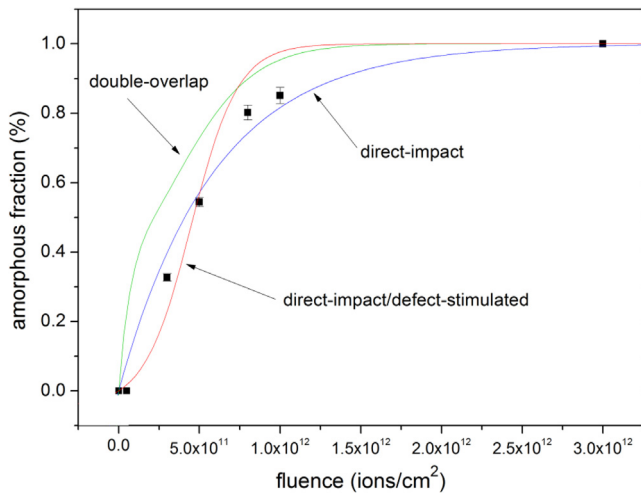


Fig. 2. Synchrotron-XRD patterns of unirradiated and irradiated samples for a range of ion fluences,  $\phi$  (in ions/cm<sup>2</sup>). The peaks labelled on the unirradiated profile correspond to the most prominent diffraction maxima of orthorhombic L-Ta<sub>2</sub>O<sub>5</sub>.



**Fig. 3.** The evolution of unit cell parameters  $a$ ,  $b$ , and  $c$ , along with the corresponding unit cell volume, as a function of ion fluence. Curves are shown only to guide the eye.



**Fig. 4.** The amorphous fraction as a function of fluence, with each of the four mathematical model fits.

The closest fit to the data is given by the simplest model, representing a direct-impact mechanism of amorphization, shown in Eq. (1). The direct-impact mechanism is associated with phase transformations originating from within each cylindrical ion track.

$$f_A = 1 - e^{-\sigma_a \phi} \quad (1)$$

In this model, the amorphous fraction,  $f_A$ , is represented in terms of the amorphization cross-section,  $\sigma_a$ , and ion fluence,  $\phi$ . A fit to the data yielded  $\sigma_a = 1.695 \times 10^{-12} \text{ cm}^2$  (169.5 nm<sup>2</sup>), which gives an amorphous track diameter of 14.7 nm, assuming a cylindrical track.

### 3.2. Raman spectroscopy

The Raman spectrum for unirradiated Ta<sub>2</sub>O<sub>5</sub> shows many Raman-active bands between 200 and 1000 cm<sup>-1</sup>, consistent with previously published data [3,7,8,68,69]. This spectrum is shown in Fig. 5, with bands labelled A through E. Peak A at 265 cm<sup>-1</sup> has been attributed to inter-polyhedral Ta-O-Ta bending [3,69,70], and peak B at 498 cm<sup>-1</sup> is associated with torsional motion within polyhedra [69]. Peaks labelled “C” correspond to symmetric Ta-O vibrations in Ta<sub>6</sub> polyhedra [3,69,71], and peak D, at approximately 845 cm<sup>-1</sup>, has been ascribed to Raman-active modes in Ta<sub>7</sub> polyhedra within  $\beta$ -Ta<sub>2</sub>O<sub>5</sub> [3]. Peak E is currently unassigned but is likely due to secondary scattering. The determination that both Ta<sub>6</sub> and Ta<sub>7</sub> polyhedra are present in the unirradiated crystalline sample is consistent with the orthorhombic structure model used to fit the XRD data.

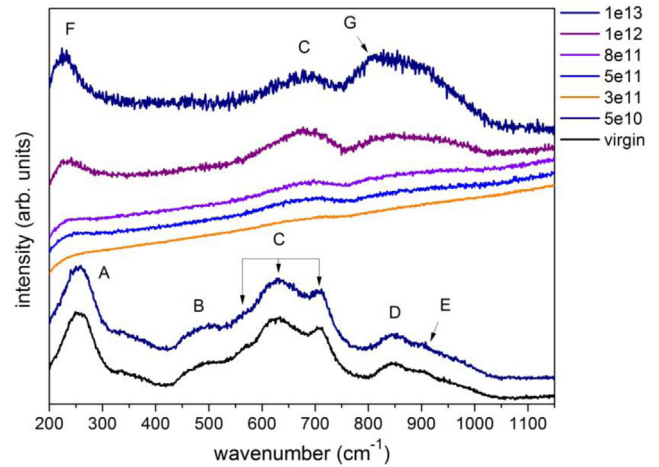


**Fig. 5.** Raman spectra for a range of fluences up to  $1 \times 10^{13}$  ions/cm<sup>2</sup>. Peaks labelled A through E correspond to Raman-active modes in crystalline Ta<sub>2</sub>O<sub>5</sub>, associated with Ta<sub>6</sub> and Ta<sub>7</sub> polyhedra. Peaks F and G correspond to Ta<sub>5</sub> polyhedra within the amorphous phase.

Little change is observed in the Raman spectra until  $3 \times 10^{11}$  ions/cm<sup>2</sup>, at which point the Raman-active modes become overwhelmed by a high intensity background. This background appears to increase linearly with wavenumber, and reaches a maximum intensity of over six times that of all other profiles. This is due to enhanced photoluminescence (PL) emission, which has been attributed to high concentrations of O vacancies in crystalline Ta<sub>2</sub>O<sub>5</sub> [72,73]. Very broad PL emission bands have been observed for O-deficient Ta<sub>2</sub>O<sub>5</sub>, centered around 695 or 705 nm depending on annealing temperature [72,73], which correspond to wavenumbers of 1409 and 1613 cm<sup>-1</sup>. The Raman spectra are therefore showing only the left-hand portion of the broad luminescence peak that reaches a maximum at over 1400 cm<sup>-1</sup>, just beyond the highest wavenumber investigated (1200 cm<sup>-1</sup>). High PL intensity is not associated with either amorphous or well crystallized Ta<sub>2</sub>O<sub>5</sub>, it has only been observed in substoichiometric crystalline samples [72]. Therefore, the intense PL background reflects high concentrations of radiation-induced O vacancies introduced into the crystalline Ta<sub>2</sub>O<sub>5</sub>. These concentrations then decrease as the proportion of the amorphous phase increases, causing the observed drop in PL intensity as fluence further increases.

As the PL intensity diminishes, several Raman-active modes are revealed. These are labelled F, C, and G in Fig. 5. Peak C is associated with the same symmetric Ta-O vibrations in Ta<sub>6</sub> polyhedra as seen in the unirradiated sample. However, peaks F and G, emerging at 220 cm<sup>-1</sup> and 815 cm<sup>-1</sup>, respectively, are both associated with Raman-active modes seen only in substoichiometric amorphous

Ta<sub>2</sub>O<sub>5</sub>. Peak F is related to Ta-Ta interaction, likely across basal planes of TaO<sub>5</sub> pyramids [3,69], and G is associated with Ta-O vibrations in the same coordination [3]. These bands are prominent only for O-deficient samples [3], and the TaO<sub>5</sub> configuration does not exist in orthorhombic Ta<sub>2</sub>O<sub>5</sub> [20]. This indicates that not only is long-range order lost during irradiation-induced amorphization (as evidenced by the XRD measurements), but the short-range order is also modified. The increase in intensity of peak G is complementary to the decrease in intensity of peak D, which is consistent with the proposal by Tsuchiya et al. [3], that amorphous Ta<sub>2</sub>O<sub>5</sub> is mostly comprised of TaO<sub>5</sub> and TaO<sub>6</sub> polyhedra and the absence of TaO<sub>7</sub>. The short-range order modification from TaO<sub>6</sub> and TaO<sub>7</sub> polyhedra only, to having a significant presence of TaO<sub>5</sub> (at the expense of TaO<sub>7</sub> [3]), suggests a loss of oxygen from the material during irradiation.

In order to evaluate the change in stoichiometry and proportion of TaO<sub>5</sub> in the amorphous material as a function of fluence, Pseudo-Voigt functions (assuming a linear background) were used to fit peaks C, G, and E, to compare the intensity contributions from TaO<sub>5</sub> (peak G) and TaO<sub>6</sub> (peak C) coordinations, while separating out contributions from secondary scattering (peak E). Area ratios were calculated, in the form  $\frac{A_5}{(A_6+A_5)}$ , where  $A_5$  is the area of peak G and  $A_6$  is the area of peak C. The results are shown in Fig. 6. The relative proportion of TaO<sub>5</sub> increases as a function of fluence, indicating an increased preference for this coordination geometry over TaO<sub>6</sub> as irradiation ensues. This suggests that O is preferentially lost from the amorphous material with increasing fluence. A previous study calculated these Raman-band intensity ratios for samples in which stoichiometry was directly measured using Rutherford backscattering spectroscopy (RBS) [3]. Using these relations, the stoichiometry of samples irradiated to the maximum fluence of  $1 \times 10^{13}$  ions/cm<sup>2</sup> was estimated to be Ta<sub>2</sub>O<sub>4.2</sub>.

### 3.3. SAXS

Samples irradiated to  $5 \times 10^{10}$  ions/cm<sup>2</sup> showed strong X-ray scattering. High intensity curved streaks were observed when the tracks were tilted with respect to the X-ray beam, consistent with high-aspect ratio damage structures. Thus, these data provide evidence of ion tracks [66,67]. Several models were used to fit this data, shown in Fig. 7, including a simple cylinder model (assuming a constant density) and a core-shell cylinder model. Both models yield very similar total track diameters of  $12.7 \pm 0.4$  nm and  $12.9 \pm 0.2$  nm, respectively, though the core-shell model provided

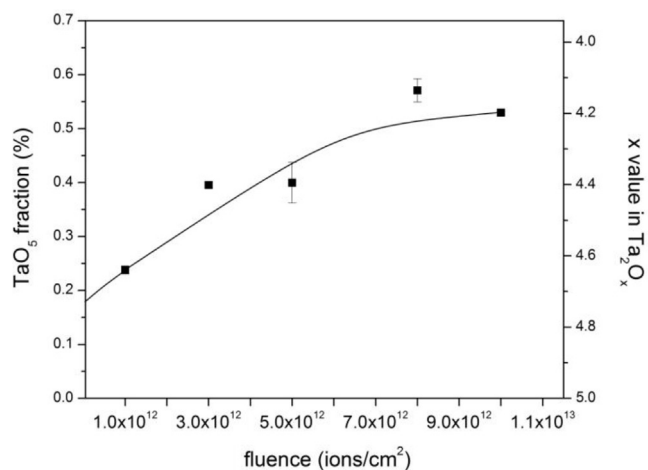


Fig. 6. Estimates for the proportion of ion-induced TaO<sub>5</sub> polyhedra (left axis) and stoichiometry of amorphous Ta<sub>2</sub>O<sub>5</sub> samples (right axis) as a function of fluence.

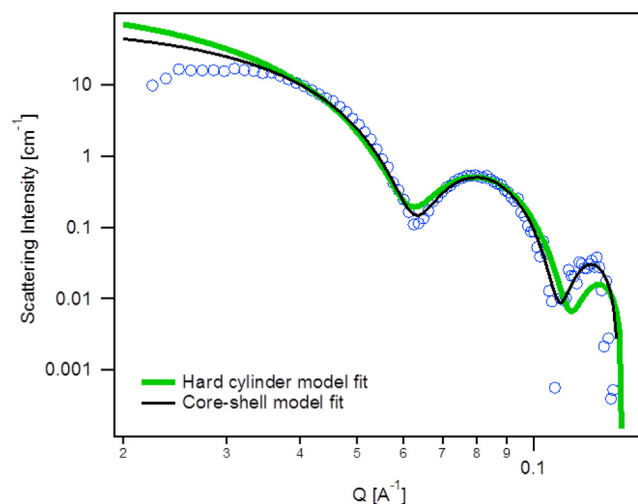


Fig. 7. Intensity profiles for Ta<sub>2</sub>O<sub>5</sub> irradiated to  $5 \times 10^{10}$  ions/cm<sup>2</sup>, showing the quality of fit for both hard cylinder and core-shell models (green line and black line, respectively). (For interpretation of the references to colour in this figure legend, the reader is referred to the web version of this article.)

a better fit to the data. This model yielded a core diameter of  $5.2 \pm 0.2$  nm, with a slightly lower density compared to the shell. The total track diameter is consistent with the direct-impact model estimate of 14.7 nm, as determined through XRD analysis.

### 3.4. TEM

TEM images were obtained from samples irradiated to  $5 \times 10^{10}$  ions/cm<sup>2</sup>, and are shown in Fig. 8. Bright-field image (a) shows ion tracks as long parallel trails of modified contrast, and (b) shows a contrast difference between inner and outer portions of each track, consistent with a core-shell morphology. The lighter inner portions are track cores, and the surrounding darker regions are track shells. Using these images, the average track core diameter was calculated by averaging 10 separate measurements, yielding a value of  $5.7 \pm 0.5$  nm, with an average total track diameter of  $11.1 \pm 0.4$  nm (errors are standard deviation values between measurements). Because images were lacking strong contrast between the track shells and matrix, this total track diameter value is considered to be a lower bound. These measurements agree well with the SAXS and XRD analysis. A close-up of a single ion track core is shown using dark-field imaging in Fig. 8c, revealing its non-cylindrical and irregular nature. This may indicate an efficient epitaxial recrystallization process during quenching. The width of each track is greater near the particle surface, possibly indicating the loss of material to the environment before melt-quenching. However, particles were crushed before TEM analysis and the observed surface may not represent the original surface during irradiation. Tracks are also seen from approximately the direction of ion irradiation in Fig. 8d, with diameters consistent with the aforementioned total track diameter measurements.

## 4. Discussion

Crystalline Ta<sub>2</sub>O<sub>5</sub> samples begin showing a diffuse amorphous background at a fluence of  $3 \times 10^{11}$  ions/cm<sup>2</sup>. Within an order of magnitude increase in fluence (up to  $3 \times 10^{12}$  ions/cm<sup>2</sup>), the material becomes completely amorphous. This fluence is quite low as compared with many other oxides, as full amorphization occurs for similar ions typically between  $5 \times 10^{12}$  and  $1 \times 10^{13}$  ions/cm<sup>2</sup> (for example, Al<sub>2</sub>O<sub>3</sub> [74], ZrO<sub>2</sub> [75], La<sub>2</sub>Ti<sub>2</sub>O<sub>7</sub> [43], Gd<sub>2</sub>Ti<sub>2</sub>O<sub>7</sub> [64], and various compositions of M<sub>2</sub>TiO<sub>5</sub> [42]). During the accumula-

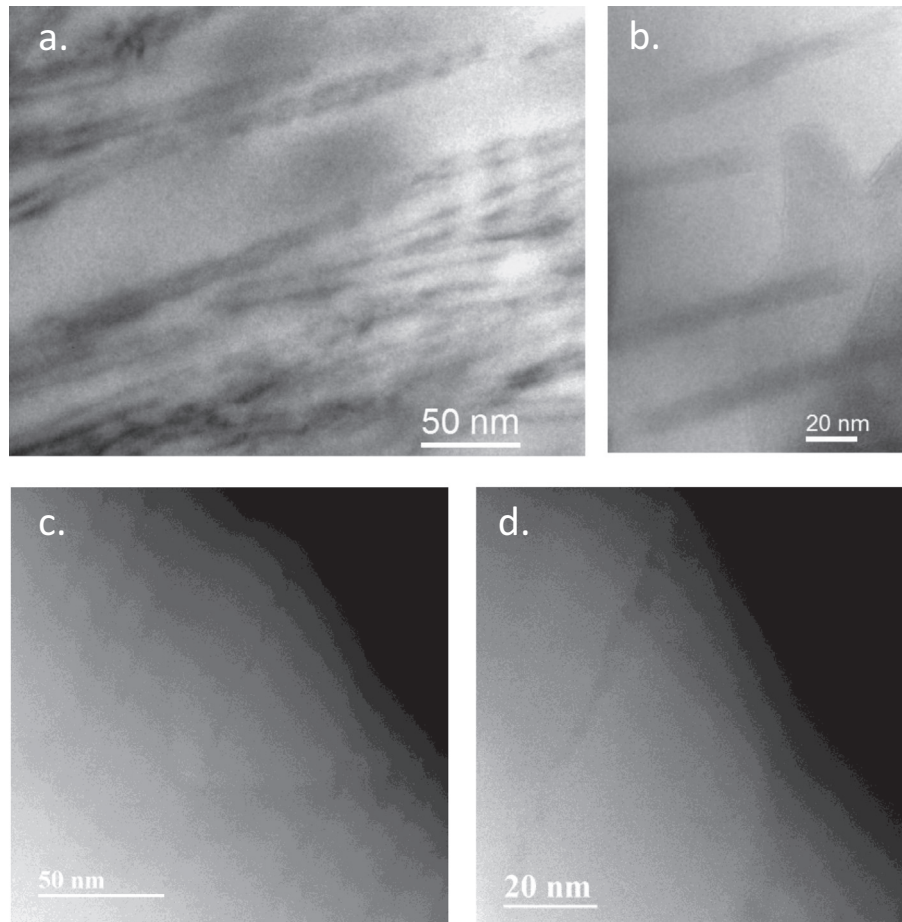


**Fig. 8.** TEM images of a  $\text{Ta}_2\text{O}_5$  particles irradiated to  $5 \times 10^{10}$  ions/cm<sup>2</sup>. Bright-field images (a) and (b) show ion tracks and their core-shell morphology. Dark-field images (c) and (d) show the irregular nature of the track cores.

tion of amorphous material, the crystalline portions of the samples undergo anisotropic lattice strain. This is likely due to stress applied by the surrounding, lower density amorphous material, but may also reflect a reorientation of Ta-O polyhedra that relates to the amorphization process. Inter-polyhedral connections along the *b*-axis are relatively weak, consisting primarily of corner-shared polyhedra. Collapse has been shown to occur first along this axis in hydrostatic pressure-induced amorphization of crystalline  $\text{Ta}_2\text{O}_5$  [5], reflecting the relative instability of the structure along this axis. As bonds break and polyhedra rearrange (for example, due to remnant thermal or pressure transients from nearby ion impact), they may preferentially tilt along the direction of the *a*-axis, thereby providing additional space in the *b* and *c*-directions. This would account for the observed anisotropic strain, as it would lead to an expansion of the *a* axis and contraction of the *b* and *c* axes. This hypothesis may be further supported by the propensity for polyhedra to become plane-sharing in amorphous  $\text{Ta}_2\text{O}_5$ , especially in substoichiometric conditions [3].

The amorphous fractions calculated from the XRD data show a continuous increase as a function of fluence. The best fit of these data was obtained using a direct-impact model, suggesting that amorphous material is formed within a single ion track, without the requirement of multiple impacts for defect accumulation. The track diameter deduced from this model is approximately 14.7 nm, which is large in comparison to many other amorphizable oxides [76–78]. This may be due to the very large and complicated crystalline structure of  $\text{Ta}_2\text{O}_5$ , which may more easily lose long range order as compared with simple oxide structures. SAXS

analysis yielded a total track diameter estimate of 12.9 nm, which is in agreement with the estimate from TEM analysis of 11.2 nm. Both techniques independently suggest the existence of a core-shell track morphology with a core size of approximately 5.2 nm (SAXS) and 5.7 nm (TEM). The direct-impact model overestimates the track diameter as calculated from SAXS and TEM data, while assuming a fully amorphous structure within the track. This suggests that the defect accumulation within the track shells, most importantly on the O sublattice, plays a significant role in the amorphization. In other words, the amorphous fraction increases at a rate comparable to the formation of large (14.7 nm) fully amorphous tracks, and because the amorphous cores are much smaller (as calculated by SAXS and TEM), the defect-rich shells must play a role in further amorphization.

At a fluence of  $3 \times 10^{11}$  ions/cm<sup>2</sup>, where amorphization is first evident in the XRD data, the Raman spectra have become overwhelmed by a broad PL emission band. This PL is not associated with the amorphous phase, but rather O vacancies existing within the crystalline  $\text{Ta}_2\text{O}_5$  structure [72]. These vacancies may be related to defect-rich track shells and/or the loss of connectivity between polyhedra resulting in dangling bonds. As point defects (in respect to Ta-O coordination polyhedra) are not dominant in the amorphous structure [3], the PL intensity diminishes as this phase is formed at the expense of the defect-rich  $\text{Ta}_2\text{O}_5$  structure. High levels of O deficiency are achieved and stabilized in the amorphous structure by a decrease in the coordination of Ta from 6 to 5, and preferential plane-sharing of polyhedra as opposed to simple corner- and edge-sharing [3]. Therefore, the observation that the

TaO<sub>5</sub>/TaO<sub>6</sub> ratio increases with fluence indicates that ion irradiation increases O deficiency. In other words, a preferential loss of oxygen occurs as a result of irradiation, leading to an O deficient coordination. The actual stoichiometry of irradiated samples was estimated using a previously published relation between the TaO<sub>5</sub>/TaO<sub>6</sub> Raman-band intensity ratio and directly measured stoichiometry values using RBS [3]. Using these data, the stoichiometry of samples irradiated to  $1 \times 10^{13}$  ions/cm<sup>2</sup> is estimated to be Ta<sub>2</sub>O<sub>4.2</sub>. Preferential loss of O during heavy ion irradiation has been observed in several oxides [45,79–81], including the direct observation of O ejection from track cores [46,47]. This anion ejection has also been observed in fluoride materials [44,48], and remains poorly understood.

## 5. Conclusion

Swift <sup>197</sup>Au ions have induced amorphization in polycrystalline Ta<sub>2</sub>O<sub>5</sub>. During this process, the crystalline unit cell undergoes an anisotropic distortion in which the network of TaO<sub>6</sub> and TaO<sub>7</sub> polyhedra that comprise the structure lose connectivity, likely along the long *b*-axis. Polyhedra may then rotate to align more closely with the *a*-axis, leading to a contraction of *b* and *c* axes while expanding along the *a* axis. The amorphous phase created during irradiation is comprised of TaO<sub>5</sub> and TaO<sub>6</sub> polyhedra in the absence of TaO<sub>7</sub>, and the ratio of TaO<sub>5</sub> to TaO<sub>6</sub> was found to increase with fluence. Because O deficiency is balanced by a transition from corner-sharing polyhedra to an edge- and plane-sharing configuration (causing a decrease in Ta coordination from 6 to 5), these data clearly indicate a loss of O during ion irradiation. The final stoichiometry of samples irradiated to  $1 \times 10^{13}$  ions/cm<sup>2</sup> is estimated to be Ta<sub>2</sub>O<sub>4.2</sub>. SAXS data suggest that ion tracks exhibit a core-shell morphology, in which the amorphous core is surrounded by a defect-rich shell. The average diameter of the track cores and shells (total track diameter) were estimated to be  $5.2 \pm 0.2$  nm and  $12.9 \pm 0.2$  nm, respectively. TEM data support these results, as images directly show the core-shell boundaries and measurements estimated core and total track diameters of  $5.7 \pm 0.5$  nm and  $11.1 \pm 0.4$  nm, respectively. These total track diameter measurements are both lower than the direct-impact model estimate of 14.7 nm, which assumes that tracks are large and fully amorphous. This observation of a core-shell morphology, along with the interrelation of amorphization and O deficiency, suggest that defects within track shells may play a significant role in the amorphization of Ta<sub>2</sub>O<sub>5</sub> under irradiation.

## Acknowledgements

This work was supported by the Office of Basic Energy Sciences of the US-DOE under Grant DE-FG02-97ER45656; NSF COMPRES under Grant EAR01-35554; and US-DOE under Contract DE-AC02-10886. We thank Professor Matzger's group for access to their Raman systems. XRD was performed at HPCAT (Sector 16), Advanced Photon Source (APS), Argonne National Laboratory. HPCAT operations are supported by DOE-NNSA under Award #DE-NA0001974 and DOE-BES under Award #DE-FG02-99ER45775, with partial instrumentation funding by NSF. HPCAT beamtime was granted by the Carnegie/DOE Alliance Center (CDAC). We would also like to acknowledge the support of NSF grant #DMR-0723032 for access to the JEOL 3100R05 electron microscope. Part of the research was performed at the SAXS/WAXS beamline at the Australian Synchrotron. PK acknowledges the Australian Research Council for financial support.

## References

- [1] W. Andreoni, C.A. Pignedoli, Ta<sub>2</sub>O<sub>5</sub> polymorphs: structural motifs and dielectric constant from first principles, *Appl. Phys. Lett.* 96 (2010) 62901, <http://dx.doi.org/10.1063/1.3308475>.
- [2] J.-J. Lee, H.-J. Kim, Y.-G. Kang, Y.-H. Kim, H.-G. Park, B.-Y. Kim, D.-S. Seo, Vertical liquid crystal orientation on amorphous tantalum pentoxide surfaces depending on anisotropic dipole-dipole interaction via ion beam irradiation, *Jpn. J. Appl. Phys.* 50 (2011) 31701, <http://dx.doi.org/10.1143/JJAP.50.031701>.
- [3] T. Tsuchiya, H. Imai, S. Miyoshi, P.-A. Glans, J. Guo, S. Yamaguchi, X-ray absorption, photoemission spectroscopy, and Raman scattering analysis of amorphous tantalum oxide with a large extent of oxygen nonstoichiometry, *Phys. Chem. Chem. Phys.* 13 (2011) 17013–17018, <http://dx.doi.org/10.1039/c1cp21310e>.
- [4] S. Ezhilvalavan, T.-Y. Tseng, Conduction mechanisms in amorphous and crystalline Ta<sub>2</sub>O<sub>5</sub> thin films, *J. Appl. Phys.* 83 (1998) 4797, <http://dx.doi.org/10.1063/1.367272>.
- [5] X. Lu, Q. Hu, W. Yang, L. Bai, H. Sheng, L. Wang, F. Huang, J. Wen, D.J. Miller, Y. Zhao, Pressure-induced amorphization in single-crystal Ta<sub>2</sub>O<sub>5</sub> nanowires: a kinetic mechanism and improved electrical conductivity, *J. Am. Chem. Soc.* (2013) 13947–13953.
- [6] P.C. Joshi, M.W. Cole, Influence of postdeposition annealing on the enhanced structural and electrical properties of amorphous and crystalline Ta<sub>2</sub>O<sub>5</sub> thin films for dynamic random access memory applications, *J. Appl. Phys.* 86 (1999) 871, <http://dx.doi.org/10.1063/1.370817>.
- [7] C. Joseph, P. Bourson, M.D. Fontana, Amorphous to crystalline transformation in Ta<sub>2</sub>O<sub>5</sub> studied by Raman spectroscopy, *J. Raman Spectrosc.* 43 (2012) 1146–1150, <http://dx.doi.org/10.1002/jrs.3142>.
- [8] Y. Zhu, F. Yu, Y. Man, Q. Tian, Y. He, N. Wu, Preparation and performances of nanosized Ta<sub>2</sub>O<sub>5</sub> powder photocatalyst, *J. Solid State Chem.* 178 (2005) 224–229, <http://dx.doi.org/10.1016/j.jssc.2004.11.015>.
- [9] Y. Yang, O. Sugino, Y. Kawazoe, Exceptionally long-ranged lattice relaxation in oxygen-deficient Ta<sub>2</sub>O<sub>5</sub>, *Solid State Commun.* 195 (2014) 16–20, <http://dx.doi.org/10.1016/j.ssc.2014.06.021>.
- [10] H. Kimura, J. Mizuki, S. Kamiyama, H. Suzuki, Extended x-ray absorption fine structure analysis of the difference in local structure of tantalum oxide capacitor films produced by various annealing methods, *Appl. Phys. Lett.* 66 (1995) 2209, <http://dx.doi.org/10.1063/1.113169>.
- [11] R. Ramprasad, First principles study of oxygen vacancy defects in tantalum pentoxide, *J. Appl. Phys.* 94 (2003) 5609–5612, <http://dx.doi.org/10.1063/1.1615700>.
- [12] C. Chaneliere, S. Four, J.L. Autran, R.A.B. Devine, Comparison between the properties of amorphous and crystalline Ta<sub>2</sub>O<sub>5</sub> thin <sup>®</sup> lms deposited on Si, *Microelectron. Reliab.* 39 (1999) 261–268.
- [13] E. Atanassova, R.V. Konakova, V.F. Mitin, J. Koprinarova, O.S. Lytvym, O.B. Okhrimenko, V.V. Schinkarenko, D. Virovska, Effect of microwave radiation on the properties of Ta<sub>2</sub>O<sub>5</sub> – Si microstructures, *Microelectron. Reliab.* 45 (2004) 123–135, <http://dx.doi.org/10.1016/j.microrel.2004.04.018>.
- [14] F.-C. Chiu, J.-J. Wang, J.Y. Lee, S.C. Wu, Leakage currents in amorphous Ta<sub>2</sub>O<sub>5</sub> thin films, *J. Appl. Phys.* 81 (1997) 6911, <http://dx.doi.org/10.1063/1.365252>.
- [15] Q. Li, H. Zhang, B. Cheng, R. Liu, B. Liu, J. Liu, Z. Chen, B. Zou, T. Cui, B. Liu, Pressure-induced amorphization in orthorhombic Ta<sub>2</sub>O<sub>5</sub>: an intrinsic character of crystal, *J. Appl. Phys.* 115 (2014) 193512, <http://dx.doi.org/10.1063/1.4879245>.
- [16] Y. Noda, B. Lee, K. Domen, J.N. Kondo, Synthesis of crystallized mesoporous tantalum oxide and its photocatalytic activity for overall water splitting under ultraviolet light irradiation, *Chem. Mater.* (2008) 5361–5367.
- [17] I.E. Grey, W.G. Mumme, R.S. Roth, The crystal chemistry of L-Ta<sub>2</sub>O<sub>5</sub> and related structures, *J. Solid State Chem.* 178 (2005) 3308–3314, <http://dx.doi.org/10.1016/j.jssc.2005.08.011>.
- [18] L.A. Aleshina, S.V. Loginova, Rietveld analysis of X-ray diffraction pattern from β-Ta<sub>2</sub>O<sub>5</sub> oxide, *Crystallogr. Rep.* 47 (2002) 415–419, <http://dx.doi.org/10.1134/1.1481927>.
- [19] C. Askeljung, B.-O. Marinder, M. Sundberg, Effect of heat treatment on the structure of L-Ta<sub>2</sub>O<sub>5</sub>, *J. Solid State Chem.* 176 (2003) 250–258, <http://dx.doi.org/10.1016/j.jssc.2003.07.003>.
- [20] N.C. Stephenson, R.S. Roth, Structural systematics in the binary system Ta<sub>2</sub>O<sub>5</sub>-WO<sub>3</sub>. V. The structure of the low-T form of tantalum oxide L-Ta<sub>2</sub>O<sub>5</sub>, *Acta Cryst.* (1971).
- [21] N.C. Stephenson, R.S. Roth, The crystal structure of the high temperature form of Ta<sub>2</sub>O<sub>5</sub>, *J. Solid State Chem.* 3 (1971) 145–153, [http://dx.doi.org/10.1016/0022-4596\(71\)90018-1](http://dx.doi.org/10.1016/0022-4596(71)90018-1).
- [22] J.L. Waring, R.S. Roth, Effect of oxide additions on polymorphism of tantalum pentoxide (system Ta<sub>2</sub>O<sub>5</sub>-TiO<sub>2</sub>), *J. Res. Natl. Bur. Stand. Sect. A* 72A (1968) 175, <http://dx.doi.org/10.6028/jres.072A.018>.
- [23] H. Hummel, R. Fackler, P. Remmert, Tantaloxide durch Gasphasenhydrolyse, Druckhydrolyse und Transportreaktion aus 2H-TaS<sub>2</sub>: Synthesen von TT-Ta<sub>2</sub>O<sub>5</sub> und T-Ta<sub>2</sub>O<sub>5</sub> und Kristallstruktur von T-, *Chem. Ber.* (1992) 551–556, <http://dx.doi.org/10.1002/cber.19921250304>.
- [24] F. Izumi, H. Kodama, A new modification of tantalum(V) oxide, *J. Less-Common Met.* 63 (1979) 305–307.
- [25] A. Fukumoto, K. Miwa, Prediction of hexagonal Ta<sub>2</sub>O<sub>5</sub> structure by first-principles calculations, *Phys. Rev. B* 55 (1997) 155–160, <http://dx.doi.org/10.1103/PhysRevB.55.11155>.

- [26] Z. Helali, M. Calatayud, C. Minot, Novel delta-Ta<sub>2</sub>O<sub>5</sub> structure obtained from DFT calculations, *J. Phys. Chem. C* 118 (2014) 13652–13658, <http://dx.doi.org/10.1021/jp503088h>.
- [27] S. Lagergren, A. Magneii, On the tantalum-oxygen system, *Acta Chem. Scand.* 6 (1952) 444–446.
- [28] X.Q. Liu, X.D. Han, Z. Zhang, L.F. Ji, Y.J. Jiang, The crystal structure of high temperature phase Ta<sub>2</sub>O<sub>5</sub>, *Acta Mater.* 55 (2007) 2385–2396, <http://dx.doi.org/10.1016/j.actamat.2006.11.031>.
- [29] Zaslavskii, No access to pdf (n.d.).
- [30] Laves, Petter, no pdf (n.d.).
- [31] I.P. Zibrov, V.P. Filonenko, Structures and phase transitions of B-Ta<sub>2</sub>O<sub>5</sub> and Z-Ta<sub>2</sub>O<sub>5</sub>: two high-pressure forms of Ta<sub>2</sub>O<sub>5</sub>, *Acta Crystallogr. Sect. B* 56 (2000) 659–665.
- [32] M. Audier, B. Chenevier, H. Roussel, L. Vincent, A. Peña, A. Lintanf Salaün, A very promising piezoelectric property of thin films. I: Monoclinic–trigonal phase transition, *J. Solid State Chem.* 184 (2011) 2023–2032, <http://dx.doi.org/10.1016/j.jssc.2011.06.001>.
- [33] C.L. Tracy, J. McLain Pray, M. Lang, D. Popov, C. Park, C. Trautmann, R.C. Ewing, Defect accumulation in ThO<sub>2</sub> irradiated with swift heavy ions, *Nucl. Instr. Meth. Phys. Res. Sect. B* 326 (2014) 169–173, <http://dx.doi.org/10.1016/j.nimb.2013.08.070>.
- [34] T. Wiss, H. Matzke, C. Trautmann, M. Toulemonde, S. Klauzunzer, Radiation damage in UO<sub>2</sub> by swift heavy ions, *Nucl. Instr. Meth. Phys. Res. Sect. B* 122 (1997) 583–588.
- [35] A. Benyagoub, Mechanism of the monoclinic-to-tetragonal phase transition induced in zirconia and hafnia by swift heavy ions, *Phys. Rev. B* 72 (2005) 94114, <http://dx.doi.org/10.1103/PhysRevB.72.094114>.
- [36] M. Lang, F. Zhang, J. Zhang, C. Tracy, A. Cusick, J. von Ehr, Z. Chen, C. Trautmann, R. Ewing, Swift heavy ion-induced phase transformation in Gd<sub>2</sub>O<sub>3</sub>, *Nucl. Instr. Meth. Phys. Res. Sect. B* 326 (2014) 121–125.
- [37] S. Hemon, V. Chailley, E. Doorhyee, C. Dufour, F. Gourbilleau, F. Levesque, E. Paumier, Phase transformation of polycrystalline Y<sub>2</sub>O<sub>3</sub> under irradiation with swift heavy ions, *Nucl. Instr. Meth. Phys. Res. Sect. B* 122 (1997) 563–565.
- [38] B. Schuster, F. Fujara, B. Merk, R. Neumann, T. Seidl, C. Trautmann, Response behavior of ZrO<sub>2</sub> under swift heavy ion irradiation with and without external pressure, *Nucl. Instr. Meth. Phys. Res. Sect. B* 277 (2012) 45–52, <http://dx.doi.org/10.1016/j.nimb.2011.12.060>.
- [39] W. Weber, Models and mechanisms of irradiation-induced amorphization in ceramics, *Nucl. Instr. Meth. Phys. Res. Sect. B* 166–167 (2000) 98–106, [http://dx.doi.org/10.1016/S0168-583X\(99\)00643-6](http://dx.doi.org/10.1016/S0168-583X(99)00643-6).
- [40] V. Kumar, D. Pratap, A. Jain, D.C. Agarwal, I. Sulania, A. Tripathi, R.J. Chaudhary, R.S. Chauhan, Crystalline to amorphous phase transition of tin oxide nanocrystals induced by SHI at low temperature, *AIP Conf. Proc.* 715 (2012) 715–716, <http://dx.doi.org/10.1063/1.4710203>.
- [41] A. Benyagoub, Investigations by X-ray diffraction of swift heavy ion induced effects in inorganic materials, *Nucl. Instr. Meth. Phys. Res. Sect. B* 225 (2004) 88–96, <http://dx.doi.org/10.1016/j.nimb.2004.03.083>.
- [42] C.L. Tracy, M. Lang, J. Zhang, F. Zhang, Z. Wang, R.C. Ewing, Structural response of A<sub>2</sub>TiO<sub>5</sub> (A=L, Nd, Sm, Gd) to swift heavy ion irradiation, *Acta Mater.* 60 (2012) 4477–4486, <http://dx.doi.org/10.1016/j.actamat.2012.05.005>.
- [43] S. Park, M. Lang, C.L. Tracy, J. Zhang, F. Zhang, C. Trautmann, P. Kluth, M.D. Rodriguez, R.C. Ewing, Swift heavy ion irradiation-induced amorphization of La<sub>2</sub>Ti<sub>2</sub>O<sub>7</sub>, *Nucl. Instr. Meth. Phys. Res. Sect. B* 326 (2014) 145–149, <http://dx.doi.org/10.1016/j.nimb.2013.10.035>.
- [44] K. Schwartz, G. Wirth, C. Trautmann, T. Steckenreiter, Ion-induced formation of colloids in LiF at 15 K, *Phys. Rev. B* 56 (1997) 10711–10714, <http://dx.doi.org/10.1103/PhysRevB.56.10711>.
- [45] A.B. Cusick, M. Lang, F. Zhang, J. Zhang, C. Trautmann, R.C. Ewing, Phase transformation and chemical decomposition of nanocrystalline SnO<sub>2</sub> under heavy ion irradiation, 2015.
- [46] V. Saikiran, N. Srinivasa Rao, G. Devaraju, G.S. Chang, A.P. Pathak, Formation of Ge nanocrystals from ion-irradiated GeO<sub>2</sub> nanocrystals by swift Ni ion beam, *Nucl. Instr. Meth. Phys. Res. Sect. B* 312 (2013) 1–6, <http://dx.doi.org/10.1016/j.nimb.2013.07.005>.
- [47] S. Takaki, K. Yasuda, T. Yamamoto, S. Matsumura, N. Ishikawa, Atomic structure of ion tracks in Ceria, *Nucl. Instr. Meth. Phys. Res. Sect. B* 326 (2014) 140–144, <http://dx.doi.org/10.1016/j.nimb.2013.10.077>.
- [48] J. Jensen, A. Dunlop, S. Della-Negra, Microscopic observations of metallic inclusions generated along the path of MeV clusters in CaF<sub>2</sub>, *Nucl. Instr. Meth. Phys. Res. Sect. B* 146 (1998) 399–404, [http://dx.doi.org/10.1016/S0168-583X\(98\)00515-1](http://dx.doi.org/10.1016/S0168-583X(98)00515-1).
- [49] M. Toulemonde, C. Dufour, A. Meftah, E. Paumier, Transient thermal processes in heavy ion irradiation of crystalline inorganic insulators, *Nucl. Instr. Meth. Phys. Res. Sect. B* 166–167 (2000) 903–912, [http://dx.doi.org/10.1016/S0168-583X\(99\)00799-5](http://dx.doi.org/10.1016/S0168-583X(99)00799-5).
- [50] M. Toulemonde, J.M. Costantini, C. Dufour, A. Meftah, E. Paumier, F. Studer, Track creation in SiO<sub>2</sub> and BaFe<sub>12</sub>O<sub>19</sub> by swift heavy ions: a thermal spike description, *Nucl. Instr. Meth. Phys. Res. Sect. B* 116 (1996) 37–42.
- [51] G. Szenes, Thermal spike model of amorphous track formation in insulators irradiated by swift heavy ions, *Nucl. Instr. Meth. Phys. Res. Sect. B* 2 (1996) 1–4.
- [52] S. Klauzunzer, Thermal-spike models for ion track physics: a critical examination, *Med. Phys.* (2008) 293–323, <http://dx.doi.org/10.1118/1.2823217>.
- [53] G. Szenes, Coulomb explosion at low and high ion velocities, *Nucl. Instr. Meth. Phys. Res. Sect. B* 298 (2013) 76–80, <http://dx.doi.org/10.1016/j.nimb.2013.01.033>.
- [54] W. Li, M.D. Rodriguez, P. Kluth, M. Lang, N. Medvedev, M. Sorokin, J. Zhang, B. Afra, M. Bender, D. Severin, C. Trautmann, R.C. Ewing, Effect of doping on the radiation response of conductive Nb–SrTiO<sub>3</sub>, *Nucl. Instr. Meth. Phys. Res. Sect. B* 302 (2013) 40–47, <http://dx.doi.org/10.1016/j.nimb.2013.03.010>.
- [55] R.L. Fleischer, P.B. Price, R.M. Walker, *Nuclear Tracks in Solids*, University of California Press, 1975.
- [56] N. Itoh, D.M. Duffy, S. Khakshouri, A.M. Stoneham, Making tracks: electronic excitation roles in forming swift heavy ion tracks, *J. Phys. Condens. Matter.* 21 (2009) 474205, <http://dx.doi.org/10.1088/0953-8984/21/47/474205>.
- [57] P. Audebert, P. Daguzan, A. Dos Santos, J.C. Gauthier, J.P. Geindre, S. Guizard, G. Hamoniaux, K. Krastev, P. Martin, G. Petite, A. Antonetti, Space-time observation of an electron gas in SiO<sub>2</sub>, *Phys. Rev. Lett.* 73 (1994) 1990–1993.
- [58] K.H. Bennemann, Ultrafast dynamics in solids, *J. Phys. Condens. Matter.* 16 (2004) R995–R1056, <http://dx.doi.org/10.1088/0953-8984/16/30/R01>.
- [59] G. Sciaini, M. Harb, S.G. Kruglik, T. Payer, C.T. Hebeisen, F.-J.M. Zu Heringdorf, M. Yamaguchi, M. Horn-von Hoegen, R. Ernstorfer, R.J.D. Miller, Electronic acceleration of atomic motions and disordering in bismuth, *Nature* 458 (2009) 56–59, <http://dx.doi.org/10.1038/nature07788>.
- [60] M. Lang, C.L. Tracy, R.L. Palomares, F. Zhang, D. Severin, M. Bender, C. Trautmann, C. Park, V.B. Prakapenka, V.A. Skuratov, R.C. Ewing, Characterization of ion-induced radiation effects in nuclear materials using synchrotron X-ray, *Techniques* (2014).
- [61] J.F. Ziegler, M.D. Ziegler, J.P. Biersack, SRIM – the stopping and range of ions in matter, *Nucl. Instr. Meth. Phys. Res. Sect. B* 268 (2010) 1818–1823, <http://dx.doi.org/10.1016/j.nimb.2010.02.091>.
- [62] A.P. Hammersley, S.O. Svensson, M. Hanfland, A.N. Fitch, D. Häusermann, FIT2D, 2005.
- [63] J. Rodriguez-Carvajal, FULLPROF Suite, 2011.
- [64] M. Lang, F.X. Zhang, R.C. Ewing, J. Lian, C. Trautmann, Z. Wang, Structural modifications of Gd<sub>2</sub>Zr<sub>2-x</sub>Ti<sub>x</sub>O<sub>7</sub> pyrochlore induced by swift heavy ions: disordering and amorphization, *J. Mater. Res.* 24 (2009) 1322–1334, <http://dx.doi.org/10.1557/jmr.2009.0151>.
- [65] T.J.B. Holland, S.A.T. Redfern, Unit cell refinement from powder diffraction data: the use of regression diagnostics 61 (1997).
- [66] B. Afra, M.D. Rodriguez, C. Trautmann, O.H. Pakarinen, F. Djurabekova, K. Nordlund, T. Bierschenk, R. Giulian, M.C. Ridgway, G. Rizza, N. Kirby, M. Toulemonde, P. Kluth, SAXS investigations of the morphology of swift heavy ion tracks in α-quartz, *J. Phys. Condens. Matter.* 25 (2013) 45006, <http://dx.doi.org/10.1088/0953-8984/25/4/045006>.
- [67] B. Afra, M. Lang, M.D. Rodriguez, J. Zhang, R. Giulian, N. Kirby, R.C. Ewing, C. Trautmann, M. Toulemonde, P. Kluth, Annealing kinetics of latent particle tracks in Durango apatite, *Phys. Rev. B* 83 (2011) 1–5, <http://dx.doi.org/10.1103/PhysRevB.83.064116>.
- [68] J.C. Sarker, R. Vasani, Y.F. Makableh, S. Lee, A.I. Nusir, M.O. Manasreh, Enhanced performance of surface modified InAs quantum dots solar cell by a sol-gel grown tantalum pentoxide antireflection coating, *Sol. Energy Mater. Sol. Cells* 127 (2014) 58–62, <http://dx.doi.org/10.1016/j.solmat.2014.03.055>.
- [69] U. Balachandran, N.G. Eror, A study of the crystal structure of B-Ta<sub>2</sub>O<sub>5</sub> by vibrational spectroscopy and X-ray diffraction, *J. Mater. Sci. Lett.* 1 (1982) 219–222.
- [70] P.S. Dopal, R.S. Katiyar, Y. Jiang, R. Guo, A.S. Bhalla, Raman scattering study of a phase transition in tantalum pentoxide, *J. Raman Spectrosc.* 31 (2000) 1061.
- [71] R.R. Krishnan, K.M. Nissamudeen, K.G. Gopchandran, V.P.M. Pillai, V. Ganesan, Effect of doping and substrate temperature on the structural and optical properties of reactive pulsed laser ablated tin oxide doped tantalum oxide thin films, *Vacuum* 84 (2010) 1204–1211, <http://dx.doi.org/10.1016/j.vacuum.2009.10.026>.
- [72] M. Zhu, Z. Zhang, W. Miao, Intense photoluminescence from amorphous tantalum oxide films, *Appl. Phys. Lett.* 89 (2006) 10–13, <http://dx.doi.org/10.1063/1.2219991>.
- [73] W. Miao, M.M. Zhu, Z.C. Li, Z.J. Zhang, Optical and electric properties of aligned-growing Ta<sub>2</sub>O<sub>5</sub> nanorods, *Mater. Trans.* 49 (2008) 2288–2291, <http://dx.doi.org/10.2320/matertrans.MRA2008137>.
- [74] A. Kabir, A. Meftah, J.P. Stoquert, M. Toulemonde, I. Monnet, Amorphization of sapphire induced by swift heavy ions: a two step process, *Nucl. Instr. Meth. Phys. Res. Sect. B* 266 (2008) 2976–2980, <http://dx.doi.org/10.1016/j.nimb.2008.03.151>.
- [75] F. Lu, J. Wang, M. Lang, M. Toulemonde, F. Namavar, C. Trautmann, J. Zhang, R. C. Ewing, J. Lian, Amorphization of nanocrystalline monoclinic ZrO<sub>2</sub> by swift heavy ion irradiation, *Phys. Chem. Chem. Phys.* 14 (2012) 12295–12300, <http://dx.doi.org/10.1039/c2cp41553d>.
- [76] M. Lang, J. Lian, J. Zhang, F. Zhang, W.J. Weber, C. Trautmann, R.C. Ewing, Single-ion tracks in Gd<sub>2</sub>Zr<sub>2-x</sub>Ti<sub>x</sub>O<sub>7</sub> pyrochlores irradiated with swift heavy ions, *Phys. Rev. B* 79 (2009) 1–9, <http://dx.doi.org/10.1103/PhysRevB.79.224105>.
- [77] J. Wang, M. Lang, R.C. Ewing, U. Becker, Multi-scale simulation of structural heterogeneity of swift-heavy ion tracks in complex oxides, *J. Phys. Condens. Matter.* 25 (2013) 135001, <http://dx.doi.org/10.1088/0953-8984/25/13/135001>.
- [78] P. Kluth, C.S. Schnorr, O.H. Pakarinen, F. Djurabekova, D.J. Sprouster, R. Giulian, M.C. Ridgway, A.P. Byrne, C. Trautmann, D.J. Cookson, K. Nordlund, M. Toulemonde, Fine structure in swift heavy ion tracks in amorphous SiO<sub>2</sub>, *Phys. Rev. Lett.* 101 (2008) 1–4, <http://dx.doi.org/10.1103/PhysRevLett.101.175503>.

- [79] A. Kabir, A. Meftah, J.P. Stoquert, M. Toulemonde, I. Monnet, M. Izerrouken, Structural disorder in sapphire induced by 90.3 MeV xenon ions, in: Nucl. Instr. Meth. Phys. Res. Sect. B 268 (2010) 3195–3198, <http://dx.doi.org/10.1016/j.nimb.2010.05.087>.
- [80] A. Iwase, H. Ohno, N. Ishikawa, Y. Baba, N. Hirao, T. Sonoda, M. Kinoshita, Study on the behavior of oxygen atoms in swift heavy ion irradiated CeO<sub>2</sub> by means of synchrotron radiation X-ray photoelectron spectroscopy, Nucl. Instr. Meth. Phys. Res. Sect. B 267 (2009) 969–972, <http://dx.doi.org/10.1016/j.nimb.2009.02.035>.
- [81] H. Ohno, A. Iwase, D. Matsumura, Y. Nishihata, J. Mizuki, N. Ishikawa, Y. Baba, N. Hirao, T. Sonoda, M. Kinoshita, Study on effects of swift heavy ion irradiation in cerium dioxide using synchrotron radiation X-ray absorption spectroscopy, Nucl. Instr. Meth. Phys. Res. Sect. B 266 (2008) 3013–3017, <http://dx.doi.org/10.1016/j.nimb.2008.03.155>.